Experimental validation of simulated metering and power loss characteristics of the rotary tubular spool valve.

Ivan Okhotnikov[a,b,*], Karem Abuowda[a], Siamak Noroozi[a], Philip Godfrey[b]

[a]*Department of Design and Engineering, Faculty of Science and Technology, Bournemouth University, Poole House, Talbot Campus, Fern Barrow, Poole, Dorset, BH12 5BB, United Kingdom*
[b]*Hydreco Hydraulics Limited, 32 Factory Road, Poole, Dorset, BH16 5SL, United Kingdom*

Abstract

This paper presents the results of numerical and experimental performance evaluation of the rotary tubular spool valve. The aim of this work is to develop further the novel design of the tubular spool valve by confirming validity of the simulation model and its results, thereby proving the valve's potential to represent a feasible and more efficient alternative to conventionally used spool valves avoiding the use of more expensive two stage valve configurations. In this research the valve performance is assessed through numerical modelling and experimental studies of metering and pressure loss characteristics of the valve. This paper demonstrates that the used valve model yields the results, which agree well with the conducted experimental study. Therefore, validation of the numerical model and the modelling results in the form of theoretical valve characteristics was accomplished. Firstly, the paper presents details of a numerical approach employed to evaluate valve performance and then analyzes the simulation results. Next, the valve performance is experimentally validated by testing a prototype valve on a hydraulic test rig capable of measuring the volume flow rate, pressure levels in up- and downstream lines of the valve over the entire spool angular stroke. Initially, average discrepancies between modelling and test results were 52.46% for the metering and 82.78% for the pressure drop function. Correcting the model geometry aimed at eliminating differences between the valve model and the practically used prototype-test rig system enabled reduction of the error between experiment and modelling by 47.75% for the pressure loss function. This confirmed validity of the simulated characteristics of the valve. The benchmark comparison of pressure losses confirmed average 71.66% energy dissipation reduction compared to the industry-available analogue valve.

Keywords:
Rotary tubular spool valve, computational fluid dynamics, experimental validation, metering characteristic, power loss characteristic, benchmark study

1. Introduction

Fluid power offers a series of advantages unavailable to other drives, especially in applications requiring significant mechanical power output. Among the assets are high power density, reliability and a lower operating cost compared to competing technologies. Power hydraulics has a wide operating bandwidth. That enables fast starts, stops, and reversals. Working fluid in these systems performs power transmission, lubricating and heat averting functions [1]. Moreover, due to the large bulk modulus of hydraulic mineral oil, fluid power is less sensitive to impact loads, provides natural damping and, thus, is more reliable than mechanical transmissions [2]. These factors have made hydraulics indispensable for high power applications and ensured its dominance among power drive technologies.

*Corresponding author
Email addresses: iokhotnikov@bournemouth.ac.uk (Ivan Okhotnikov), kabuowda@bournemouth.ac.uk (Karem Abuowda), snoroozi@bournemouth.ac.uk (Siamak Noroozi), pgodfrey@hydreco.com (Philip Godfrey)

Nomenclature	
Latin	
A	Area, mm^2
A_v	Van Driest coefficient
C_d	Discharge coefficient
$C_{\varepsilon 1}$, $C_{\varepsilon 2}$, C_μ, C_B	Constants in the $k-\varepsilon$ model
d, D	Diameter, mm
D_h	Hydraulic diameter, mm^2
f_1, f_2, f_μ	Lam and Bremhost's damping functions in $k-\varepsilon$ turbulence model
k	Turbulent kinetic energy, m^2 s^{-2}
K	Karman constant
l, L	Length, characteristic length, mm
p	Pressure, MPa
P	Power, W
Q	Volume flow rate, l min^{-1}
R_T, R_y	Turbulence and velocity-average Reynolds number
Re	Reynolds number
S	Perimeter, mm
t	Time, s
u_i	The i-th component of the fluid velocity vector, m s^{-1}
u^+	Dimensionless longitudinal velocity
v, V	Average, characteristic velocity, m s^{-1}
y	Distance from the wall surface, m
y^+	Dimensionless wall distance
x_i	The i-th component of the coordinate vector, m
Greek	
δ_{ij}	Kronecker function
ε	Turbulent dissipation rate, m^2 s^{-2}, strain
μ	Dynamics viscosity, Pa s
μ_t	Turbulent eddy viscosity coefficient
ν	Kinematic viscosity, m^2 s^{-1}
ρ	Density, kg m^{-3}
σ_k, σ_ε, σ_B	Constants in the $k-\varepsilon$ model
τ_{ij}	Reynolds stress tensor, MPa
τ_w	Wall shear stress, MPa
ϕ	Spool angular position, °
Notation	
$\overline{x}$	Mean value of x
Acronyms	
AEM	Asynchronous Electric Motor
CAD	Computer Aided Design
CFD	Computational Fluid Dynamics
DAS	Data Acquisition System
FM	Flow Meter
PRV	Pressure Relief valve
PT	Pressure Transducer
RTSV	Rotary Tubular Spool Valve
SM	Stepper Motor
TT	Torque Transducer
VAC	Volts of Alternating Current
VDC	Volts of Direct Current
VFD	Variable-Frequency Drive

However, fluid power possesses several drawbacks. Tight clearances between mechanical parts require extremely clean working fluid free from solid particles, dissolved gasses and air. It necessitates regular and strict supervision of the oil's contamination level during an exploitation period. Other shortcomings are low flexibility and high non-linearity of hydraulic control relative to electromagnetic counterparts [1]. Hydraulics is also prone to oil leakage through seals, mechanical contacts and connections [3], which can cause spillages and environmental pollution.

The presence of valves modulating the output velocity of the hydraulic actuator remains the main design feature of the state of the art power hydraulic systems due to robustness and relatively low cost of this solution [4]. Flow- and pressure-regulating valves enable a link between the source of hydraulic power and its consumers, implement complex logic of actuators operation in a working cycle. The actuator's speed regulation is fulfilled through throttling adjustment, which realized by changing the valve's spool position. The spool position influences an orifice area, which in turn determines valve's hydraulic resistance. The flow rate to the actuator as well as its output velocity changes according to this area.

The common trait of valve-controlled systems is prevalence of throttling losses due to a resistive nature of flow regulation. Since the flow regulation is being fulfilled by restraining the flow inside the valve, excessive fluid power is dissipated in a form of vortices with substantial viscous friction losses and heat generation in them. These result in poor energy efficiency of the valve as well as the entire hydraulic system it is installed in. The review of the industrial state-of-the-art and research advancements in development of direct drive proportional spool valves

[5] confirms optimisation of the flow paths through the valve to lessen flow disturbances is viable, well known and tested technique to solve efficiency issues in valves and reduce pressure losses.

Judging by flow streamlines in the conventionally used spool and seat valves [6], [7], [8], [9], [10], [11], it has been concluded that, firstly, exact geometry of the valve is a sole factor defining flow trajectories, pressure losses and hence efficiency of the valve; secondly, streamlining flow paths is a way to improve efficiency of a valve; and finally, the easiest way to implement streamlining is to remove unnecessary turns and sudden cross-sectional changes of flow paths, which are in abundance in linear spool valves. The most obvious way to keep the flow route smooth is to rid of sudden U-turns. These considerations let to infer that rotary valves could provide more streamlined flow trajectories and ease of valve operation. Unlike conventional linear spool configurations, a rotating spool design especially with a hollow spool would create a much smaller net area of surfaces subjected to the flow forces, hence decreasing power consumption of a valve driving mechanism.

So far, employment of rotary spools industrially is limited to manually driven on-off ball valves, flow dividers, plug and steering valves, which are used in the steering systems of wheeled vehicles [12]. In rotary ball valves, usually a rotary spool is spherical in a cross section with drilled through-holes serving as flow paths. In valves with cylindrical spools, flow paths are milled on the external cylinder of the spool, imposing sudden changes in direction and a cross sections of flow paths. Often these valve structures still include undesirable U-turns in flow trajectories [13], [14], [15], [16], [17].

Among multitude patents dedicated to the rotary valve structures, there are design solutions suggesting a tubular spool as the main throttling part. Embodying the approach of mobile surfaces minimisation and using rotary control motion, these concepts represent a promising and under-studied class of control valve designs suitable for high-power hydraulics applications. The first found patents proposing such structures were filed in the middle of the last century by Husley and Erwin as rotary sleeve valves [18] and [19].

The present research aims at validating the used methodology to obtain CFD simulated performance characteristics of the previously suggested design of the rotary tubular valve, thereby, confirming its flow controlling capabilities and potential to improve controllability and energy efficiency of spool valves. Overall, these would allow to develop further this promising design and to prove that rotary spool valves is a viable competitor to conventional linear spool valves in terms of metering capabilities and energy efficiency.

2. Rotary tubular spool valve

2.1. Design

The design of the rotary tubular spool valve (RTSV) and theoretical analysis of flow physics within it have been reported in details in the authors' previous work [20]. The current research investigates the same valve structure, although the down scaled version, which had enabled experiments on a test rig described in the following sections.

The cut section in the figure 1 illustrates the RTSV design. The oil enters the RTSV through the circular inlet area A_{in}. Then, it flows into the central chamber of the spool 1. The chamber is formed by spool's internal cylindrical and conical surfaces and the circular area A_1. From the central chamber the oil passes through two throttling orifices, which are created by overlapping openings on the spool 1 and the sleeve 2, see the figure 1. Next, the oil finds its way from the orifices to the annular oil collecting channel, or chamber, with the cross-sectional area of A_{an}, which encircles the sleeve. The collecting chamber is connected to the outlet hydraulic port with the circular area A_{out}, which is designed to be equal to A_{in}.

To keep hydraulic disturbances to the flow as small as possible, the cross-sectional area of the entering flow A_{in} should be maintained throughout valve's internal passages up to the exit port with the area A_{out}. This approach results in the design criterion for selecting cross-sectional areas of the valve's channels.

Since there are two throttling orifices on the spool and the total flow is split in two jets, the annular area of the flow in the collecting chamber A_{an} needs to be equal to a half of the inlet flow's cross-sectional area A_{in}, i.e.

$$A_{in} = A_{out} = 2A_{an}. \tag{1}$$

At any moment the tubular spool is exposed to the pump pressure p_p acting on the spool's circular surface A_1. This creates the extruding force F_{ex} that pushes the spool out from the valve body.

$$F_{ex} = p_p A_1 \tag{2}$$

To compensate this force and to locate the spool in a certain axial position, the oil is directed through the axial channel inside the the spool to its back chamber. There, the oil acts on the annular area A_2 with the pump pressure p_p, which creates the compensating force F_{comp}.

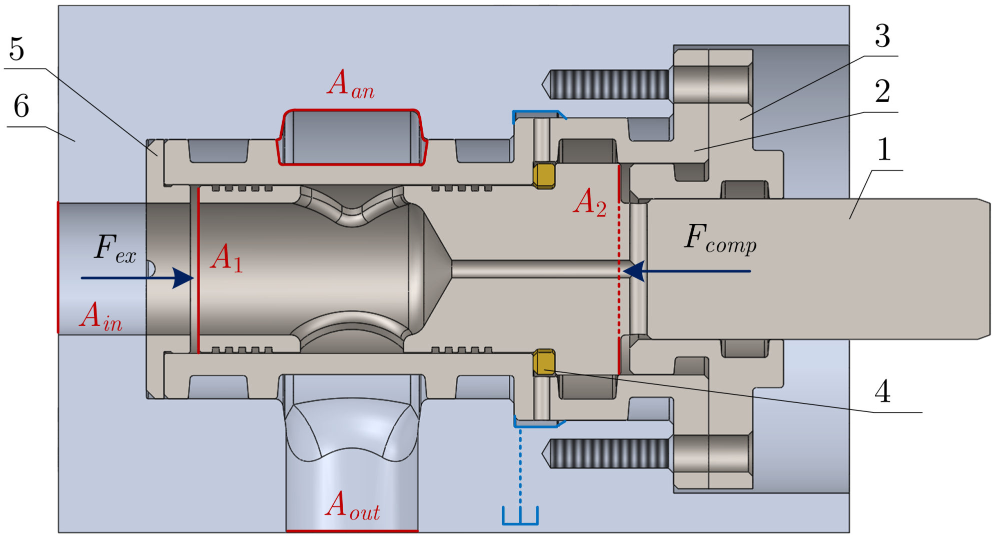

Figure 1: The cutaway section of the RTSV. Original parts: 1 – spool, 2 – sleeve, 3 – lid, 4 – thrust bearing, 5 – guiding sleeve, 6 – valve body. The region inside the spool to the right of the area A_1 – the spool central chamber or cavity. The annular region with the cross section of A_{an} – the cross-section of the single branch of the collecting channel or chamber. A_{in} and A_{out} – inlet, supply and outlet, service ports respectively. A_2 – the annular area of the spool back, or compensating chamber.

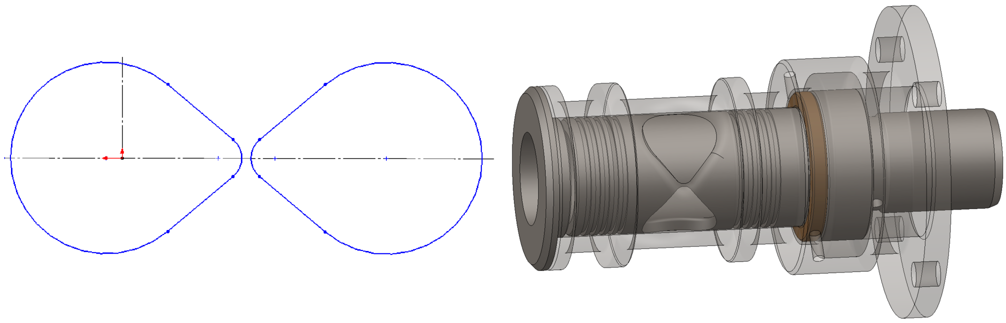

(a) ϕ = 0°, fully closed.

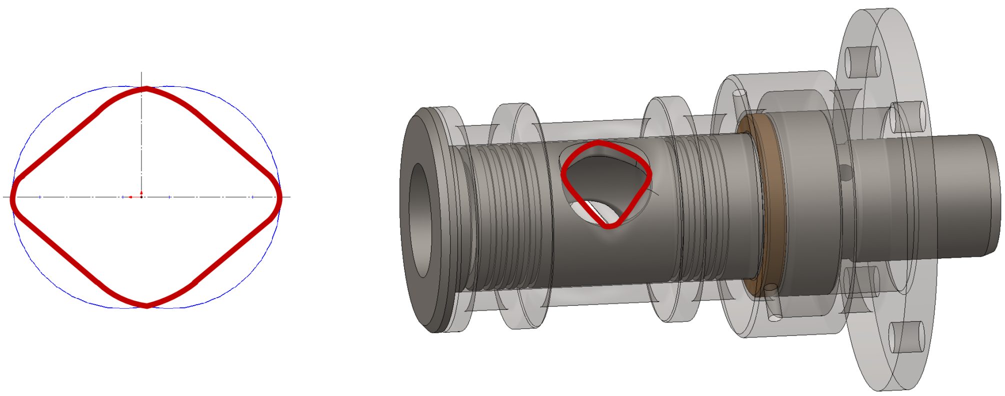

(b) ϕ = 90°, fully open.

Figure 2: The single throttling orifice at the extreme states. Left – overlap of the unfolded throttling profiles of the spool and sleeve openings. Right – location of the single throttling orifice on the spool-sleeve assembly.

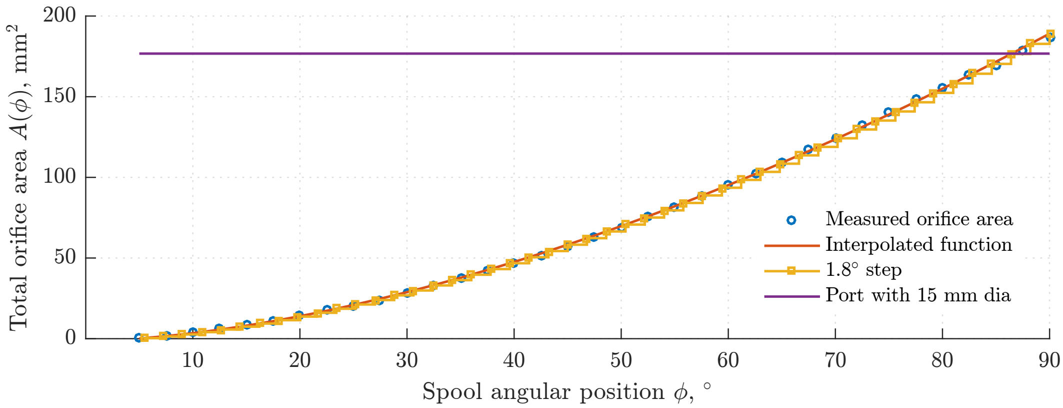

Figure 3: The total orifice area function, $A(\phi)$.

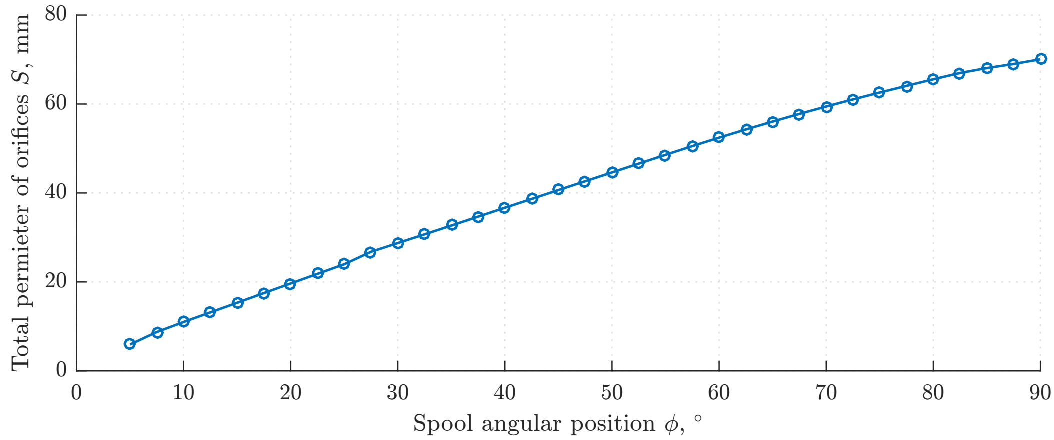

Figure 4: Total perimeter of the throttling orifices, $S(\phi)$.

$$F_{comp} = p_p A_2 \tag{3}$$

Therefore, assuming pressure levels are equal in the spool central and the back chambers, the design criterion for selecting areas A_1 and A_2 as well as ensuring spool axial stabilization is

$$\begin{gathered} F_{comp} \geq F_{ex} \\ A_2 \geq A_1 \end{gathered} \tag{4}$$

If the annular area A_2 exceeds the circular area A_1, the compensating force surpasses the ejecting force, i.e. $F_{comp} > F_{ex}$. In this case, the spool is pushed against the brass thrust bearing 4 in the figure 1. The bearing's material needs to ensure a low friction pair between the steel or aluminum spool and the bearing.

The thrust bearing features radial grooves to allow the oil leakage from the spool-sleeve clearance to drain to the tank. In the figure 1 the groove, which is cut in the body 6 and is outlined in blue, collects this leakage and drains it to the tank. The drainage channel also collects the oil flowing from the spool back chamber through the sleeve's groove of the sealing rings. Combined internal leakage from these two paths enables hydrodynamic bearing on spool and thrust bearing mating surfaces.

The guiding sleeve 5 serves to facilitate dismantling of the valve in case replacement of any internal parts is needed. Semi-circular cuts on the sleeve bottom plane can be used to pull all valve inner parts from the body 6. The lid 3 ensures all immovable parts are securely fixed by tightening screw fasteners to designated threaded blind holes on the housing 6.

2.2. *Opening area*

The throttling pair in the figure 2 performs regulation of the flow area and, hence, the flow rate passing through the RTSV. The flow rate is directly proportional to the overlap area between the slots of the rotary actuated spool and the static sleeve. The total area of the throttling orifices varies in a range between the fully closed and full open states shown in the figures 2a and 2b respectively. Therefore, the angular position of the spool ϕ in the sleeve defines the openings' overlap, the total orifice area A and the resultant oil's flow rate Q.

The total orifice area is also a function of each window profile. In the current research, the shape of openings was chosen to be the same for the spool and the sleeve, with areas chosen according to above mentioned design criteria, i.e. the maximum total orifices area at the fully open state is designed to be as close as possible to the inlet flow cross section ensuring the least resistance to the flow.

The openings on the sleeve and the spool form the orifice with the total opening area function $A(\phi)$ shown in the figure 3. The increase of the area is nonlinear with a more gradual increment at lower angles of opening. The slow non-linear change in the area at the start of actuation is a special design feature of the RTSV. The dependency at $\phi > 50°$ of the spool angular position is steeper, reaching the total orifice opening of 186.99 mm^2. The graph also includes the area of the hydraulic inlet port with the diameter of 15 mm, which results in the inlet flow cross section of 176.71 mm^2. The step-wise line on the figure 3 illustrates the area increase in the case the spool position is defined with a conventional stepper motor with 1.8° step. Additionally, the orifices's perimeter was measured, see the figure 4, to enable Reynolds number estimation in the following section.

3. CFD modelling

3.1. Turbulence model

In the considered application of the RTSV, which is high pressures and high flow rates, the fluid flow inside the valve tends to be turbulent. In the used CAD-embedded CFD software, FloEFD suit, the Favre-averaged Navier-Stokes equations are used, where the effects of the flow turbulence on the mass-averaged flow parameters are considered. The applied Favre averaging method also accounts for fluctuations of fluid density and temperature [21].

To close the system of Navier-Stokes equations, transport equations for the turbulent kinetic energy and its dissipation rate are employed, the so-called $k-\varepsilon$ model [22]. The adopted model meets accuracy and reliability requirements in the considered valve study and performs satisfactorily in solving fluid power problems [23].

In FloEFD the classical two-equations $k-\varepsilon$ empirical model for simulating turbulence effects in fluid flow CFD simulation [21] is used as it requires the minimum amount of additional information to define the flow [24]. The modified $k-\varepsilon$ turbulence model with damping functions [25] describes laminar, turbulent, and transitional flows of homogeneous fluids consisting of the following turbulence conservation laws [26]:

$$\frac{\partial \rho k}{\partial t} + \frac{\partial \rho k u_i}{\partial x_i} = \frac{\partial}{\partial x_i}\left(\left(\mu + \frac{\mu_t}{\sigma_k}\right)\frac{\partial k}{\partial x_i}\right) + \tau_{ij}^R - \rho\varepsilon + \mu_t P_B \quad (5)$$

$$\frac{\partial \rho \varepsilon}{\partial t} + \frac{\partial \rho \varepsilon u_i}{\partial x_i} = \frac{\partial}{\partial x_i}\left(\left(\mu + \frac{\mu_t}{\sigma_\varepsilon}\right)\frac{\partial \varepsilon}{\partial x_i}\right) + C_{\varepsilon 1}\frac{\varepsilon}{k}\left(f_1 \tau_{ij}^R \frac{\partial u_i}{\partial x_j} + C_B \mu_t P_B\right) - f_2 C_{\varepsilon 2}\frac{\rho\varepsilon^2}{k} \quad (6)$$

Here P_B represents turbulence generation due to buoyancy and can be written as

$$P_B = -\frac{g_i}{\rho\sigma_B}\frac{\partial \rho}{\partial x_i}, \quad (7)$$

where g_i is the component of gravitational acceleration in direction of x_i. The empirical $k-\varepsilon$ constants have the following typical values [22]: $\sigma_k = 1$, $\sigma_B = 0.9$, $\sigma_\varepsilon = 1.3$, $C_\mu = 0.09$, $C_{\varepsilon 1} = 1.44$, $C_{\varepsilon 2} = 1.92$ and constant $C_B = 1$ if $P_B > 0$, and 0 otherwise.

Following Boussinesq assumption, the Reynolds-stress tensor for Newtonian fluids has the following form:

$$\tau_{ij}^R = \mu\left(\frac{\partial u_i}{\partial x_j} + \frac{\partial u_j}{\partial x_i} - \frac{2}{3}\delta_{ij}\frac{\partial u_k}{\partial x_k}\right) - \frac{2}{3}\delta_{ij}\rho k. \quad (8)$$

Here δ_{ij} is the Kronecker delta function (it is equal to unity when $i = j$, and zero otherwise), μ is the dynamic viscosity coefficient, k is the turbulent kinetic energy and μ_t is the turbulent eddy viscosity coefficient, which is determined from

$$\mu_t = \frac{f_\mu C_\mu \rho k^2}{\varepsilon}. \quad (9)$$

Here f_μ is the turbulent viscosity factor. It is determined by the expression

$$f_\mu = \left(1 - e^{-0.0165R_y}\right)^2 \left(1 + \frac{20.5}{R_T}\right), \quad (10)$$

$$R_y = \frac{\rho\sqrt{k}y}{\mu}, \quad (11)$$

$$R_T = \frac{\rho k^2}{\mu\varepsilon} \quad (12)$$

Lam and Bremhorst's damping functions f_μ, f_1, f_2 decrease turbulent viscosity and turbulence energy and increase the turbulence dissipation rate when the Reynolds number R_y based on the average velocity of fluctuations and distance from the wall becomes too small. When $f_\mu = 1$, $f_1 = 1$, $f_2 = 1$ the approach obtains the original $k - \varepsilon$ model.

3.2. Wall function

To simulate fluid boundary layer effects near solids within the $k - \varepsilon$ model and to evaluate skin friction in these regions a "wall function"' approach [27] is utilized. Instead of a logarithmic profile, the FloEFD employs Van Driest's profiles [28]. Additionally, a "two-scale wall functions" approach to describe a turbulent boundary layer and to fit a boundary layer profile relative to the main flow's properties is employed [24].

For the sufficient number of cells across the boundary layer, more than 10, the simulation of laminar boundary layers is done via Navier-Stokes equations as part of the core flow calculation. For turbulent boundary layers proceeding from the Van Driest mixing length [28], the FloEFD uses following dependency of the dimensionless longitudinal velocity u^+ on the dimensionless wall distance y^+ [24]

$$u^+ = \frac{u}{\sqrt{\frac{\tau_w}{\rho}}} = \int_0^{y^+} \frac{2d\eta}{1 + \sqrt{1 + 4K^2\eta^2\left(1 - e^{-\frac{\eta}{A_v}}\right)^2}}. \quad (13)$$

Here $K = 0.4504$ is the Karman constant and the Van Driest coefficient is $A_v = 26$.

3.3. Mesh

The fluid subdomain was extracted from the geometric model of the RTSV. Then, the fluid domain was split into cells with adjustable resolution. The governing partial differential equations, that are the Navier-Stokes and transport equations, were solved in nodes, in centres of the mesh cells. The FloEFD solves the governing equations with a discrete numerical technique based on the finite volume discretization method as it satisfies requirements of conservation nature of the governing differential equations.

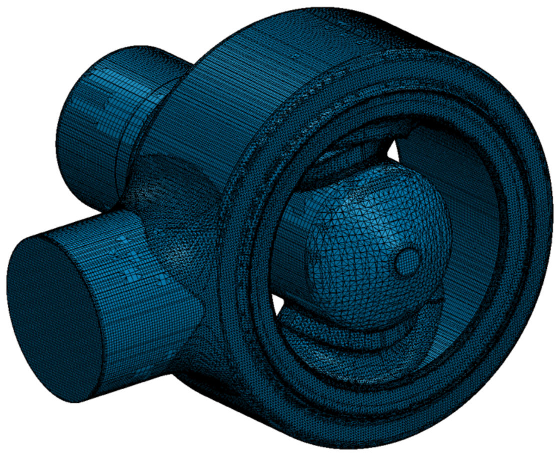

Figure 5: The mesh of the fluid subdomain with ≈ 1 million fluid cells.

The cells are rectangular parallelepipeds with orthogonal faces, which are parallel to the specified axes of the Cartesian coordinate system, see the figure 5. The near-boundary cells are fractions of the original parallelepiped cells that are cut by the solid matter geometry boundary. Thus, the resulting near-boundary cells are polyhedrons with both axis-oriented and arbitrary oriented plane faces, partial cells. All physical and inertial parameters are referred to the mass centres of the cells within the control volume [22].

The module uses the immersed body meshing approach and provides the structured and uniformed Cartesian mesh with an irregular distribution of the mesh cells, which results in the faster calculation of mesh-based information, speeds up the search for data associated with neighbour cells and has been shown to deliver the lowest local truncation error when the Navier-Stokes equations are discretized onto the mesh. The approach also simplifies navigation on the mesh and to ensure robustness of the differencing scheme by the absence of secondary skewed faces [29].

The FloEFD built-in mesh generating algorithms enable on-the-fly mesh optimisation and results in the fine enough mesh for purposes of valve designing and simulation without resorting to any further mesh refinement. In these parametric studies, the minimum gap size and minimum wall thickness of the mesh were assigned to 1 mm and 0.01 mm respectively. Both parameters influence the characteristic cell's size and computational domain resolution in narrow channels. FloEFD generates the mesh to have a minimum of two

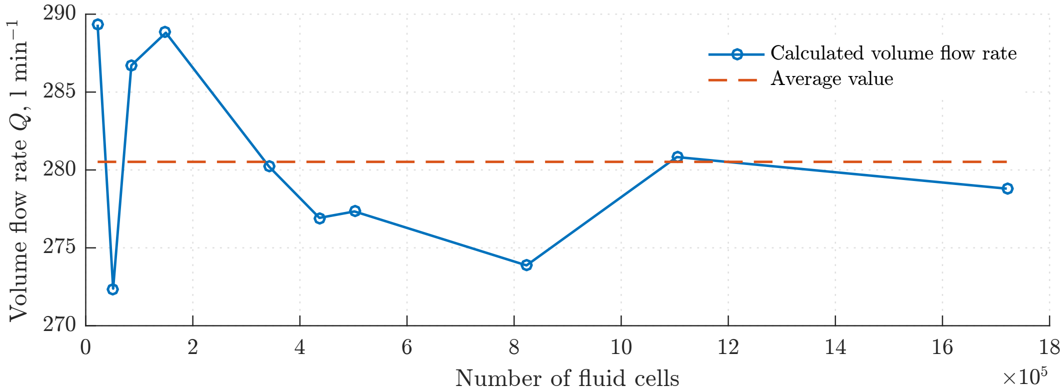

Figure 6: Grid independence study results. The mean value $\overline{Q}$ = 280.461 l min^{-1}, the standard deviation σ = 5.971 l min^{-1}, which is 2.13% deviation from the mean value.

cells per the specified minimum gap size. The wall thickness parameter defines the refinement level of the mesh at the fine geometrical elements such as sharp edges and small protrusions [22].

Applied solution-adaptive refinement process allows splitting the mesh cells into the high-gradient flow regions, which cannot be resolved prior to the calculation and merging the mesh cells in the low-gradient regions. It serves to minimize the spatial error arising from the discretization of the governing differential equations [29]. Areas adjacent to the throttling orifices were subjected to further automated solution adaptive refinement, which resulted in the increasing the number of fluid cells in areas with significant changes of variables, i.e. flow restrictions.

3.3.1. Grid independence

A grid independence study has been conducted for the case of $\Delta p = 1$ MPa pressure drop between inlet and outlet openings of the valve and the spool angular position $\phi = 90°$, the full open state. For the specified conditions, several meshes have been created differing in a number of fluid cells from 22 000 to 1 700 000. The mean value of the computed flow rate between different meshes is equal to $\overline{Q} = 280.461$ l min^{-1} with 3.13% fluctuations of the extreme values around the average one.

The standard deviation is 5.971 l min^{-1}, which is considered as an acceptable value to conclude that the obtained values ensure the convergence of the solution regardless of the mesh resolution. The applied mesh resolutions provide acceptable accuracy of the computed results. The result of the mesh independence study is shown in the figure 6.

The meshing algorithm for further parametric studies was selected providing on average 1.1 million fluid cells and three million partial cells on the surfaces bordering with solid matter. The maximum cell size of the basic mesh before the refinement process commences is 0.8 mm. The chosen meshing setting guarantees a reasonable trade-off between computational time and accuracy for the simulations described further.

3.4. Boundary conditions

The specification of the boundary conditions consists of assigning the desired magnitude of the flow parameters to the fluid subdomain's openings and establishes the hydraulic problem to be solved by the FloEFD. In this study, a wall roughness and slip conditions were not imposed, there were no leakages through external sealing lids of the valve's fluid domain.

The first objective is to gain an understanding of the hydraulic performance of the valve and to predict areas, which would need further geometrical optimisation to reduce hydraulic pressure losses. A feature of particular interest is the valve's discharge coefficient. The coefficient as well as the orifice area depends on the spool angular position. These would complete geometrical description of the valve and allows further mathematical modelling of the valve performance.

In parametric simulations, Dirichlet boundary conditions for the steady state fluid flow were used. Namely, boundary conditions for the valve inlet were selected as the static pressure of p_{in} = 0.35 MPa, 0.6 MPa and 1.1 MPa. The valve outlet opening was subjected to the invariant static pressure of p_{out} = 0.1 MPa. It corresponds to a pressure level in an unpressurized oil tank.

Simulation type	Internal steady-state flow simulation
Geometric model	Discrete spool openings ϕ = 10° to 90° with 5° step
Fluid model	Single-phase flow, mineral hydraulic oil ISO VG 32 at 45 °C · $\rho = 850\,\mathrm{kg\,m^{-3}}$ · $\nu = 29$ cSt, · $\mu = 24.68$ cP
Mesh	Adaptive finite volume discretization, rectangular parallelepipeds with initial maximum size 0.8 mm, number of cells ≈ 1.1 million
Turbulence model	$k - \varepsilon$ turbulence model
Boundary conditions	Metering characteristic Static pressure at the inlet and the outlet: · p_{in} = 0.35 MPa, 0.6 MPa and 1.1 MPa · p_{out} = 0.1 MPa Power loss characteristic: Volume flow rates across the RTSV: · $Q = 25\,\mathrm{l\,min^{-1}}$ to $275\,\mathrm{l\,min^{-1}}$ with the $25\,\mathrm{l\,min^{-1}}$ increment Other simulation conditions: · No-slip, smooth, adiabatic wall · Two-scale wall function · Turbulence intensity 2% · Turbulence length 0.1 mm · Leakages in clearances are neglected

Table 1: Preprocessing settings of the CFD modelling.

Thus, the boundary condition of the adopted pressure drop makes up a set of Δp = 0.25 MPa, 0.5 MPa and 1 MPa pressure differentials. The magnitudes of the pressure differential were selected according to an usual margin of pressure levels in load sensing systems, which is in a range 10-20 bar [30], [31].

This set of hydraulic boundary conditions provided varying values of the pressure difference, dictating the volume flow rate passing through the orifice. For each variation of the specified input, the angular position of the spool was added as the geometrical parameter varying from 10° to full open state of 90° with a 5° step.

The boundary conditions at the inlet and outlet also included the turbulent quantities, which in this study were the turbulence intensity of 2% and the turbulence length scale, the hydraulic diameter of the inlet and outlet.

3.5. Oil model

The oil used in the CFD study is the petroleum-based anti-wear hydraulic mineral oil, viscosity grade 32. It has been treated as a compressible fluid, i.e. viscosity- and density-temperature functions were used by the FloEFD solver, although the temperature increase has been proven to be local in small areas next to the throttling edges [32].

The temperature field in the fluid subdomain is non-uniform. The initial oil temperature was taken equal to T_{in} = 318 K(45 °C) that corresponded to normal operational conditions of fluid power systems as well as intended test conditions. Oil properties correlating to this value of oil temperature [33] as well as other preprocessing settings of the CFD model are summarized in the table 1.

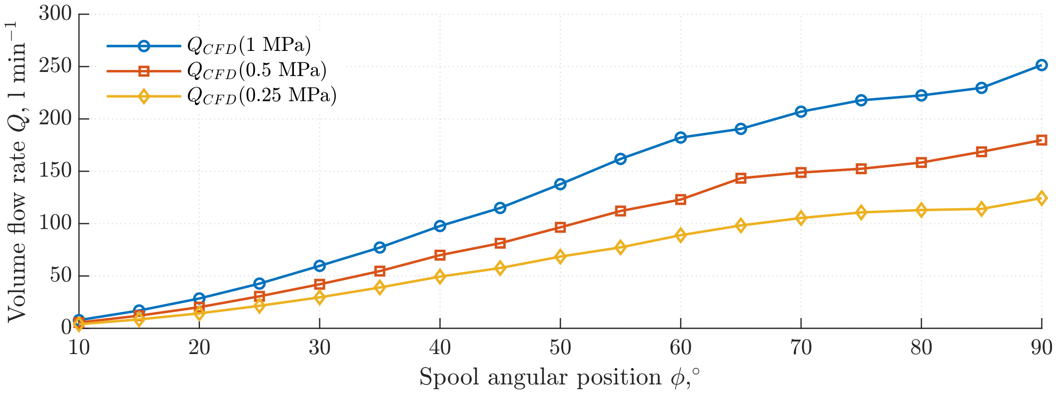

Figure 7: Modelled metering characteristic $Q(\phi)$ at Δp = 0.25; 0.5; 1 MPa

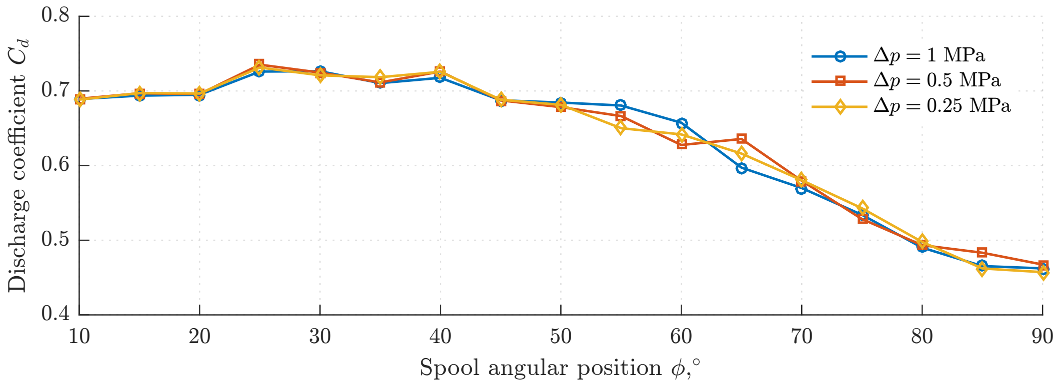

Figure 8: Discharge coefficient $C_d(\phi)$ at Δp = 0.25; 0.5; 1 MPa

3.6. Modelling results

3.6.1. Metering characteristic

During the CFD simulation studies of the valve, the spool angular position is considered as the main geometric parameter ranging from ϕ = 10° to 90° with an increment of 5°. The pressure drop across the orifice had definite values of Δp = 0.25 MPa, 0.5 MPa and 1 MPa. The volume flow rate $Q_{CFD}(\phi)$ as a function of the spool position has been simulated for the specified pressure drops. Interpolated plots for discrete data points of CFD calculated flow rates are illustrated in the figure 7.

The CFD simulated volume flow rate Q_{CFD} increases non linearly as the orifice area grows. From ϕ = 25° to 60° of the spool angular position the volume flow rate exhibits steeper rise comparing with the regions of extreme spool positions. According to the simulated results, domains close to the maximum and minimum spool positions have more gradual flow rate gains. This benefits controllability of a hydraulic actuator at small and maximum speed regimes.

3.6.2. Discharge coefficient

Simulated flow rate characteristic Q_{CFD} of the valve has allowed calculation of the discharge coefficient of the orifice for any given spool angular position according to the Bernoulli equation.

$$C_d = \frac{Q_{CFD}}{A(\phi)}\sqrt{\frac{\rho}{2\Delta p}} \tag{14}$$

For every pressure drop across the valve, computed discharge coefficient curves on the figure 8 follow the same trend and effectively coincide. Regardless of the imposed pressure differentials, discharge coefficient curves decrease as the valve opens. The maximum value of the coefficient is $C_{d.max}$ = 0.735 at ϕ = 25°, the minimal value is $C_{d.min}$ = 0.457 at the valve's open state, ϕ = 90°. With the predetermined orifice area and the discharge coefficient relation, hydraulic behaviour

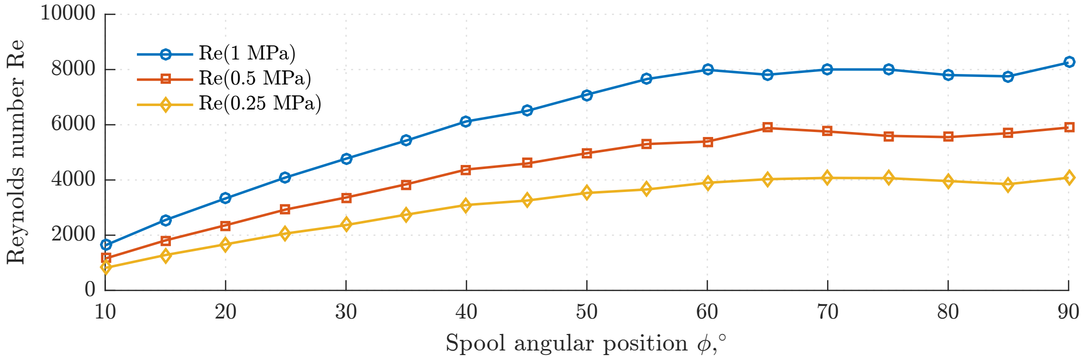

Figure 9: Reynolds number function $\mathrm{Re}(\Delta p, \phi)$

of the valve can be predicted for any operational regime of the hydraulic system.

Since the $C_d(\phi)$ function does not heavily depend on the imposed pressure differential Δp, any curve can be used further. In the following sections the $C_d(\Delta p = 1\,\mathrm{MPa})$ is used. Based on the found $A(\phi)$ function, see the figure 3, it is possible to predict the theoretical metering characteristic $Q_{th}(\phi, \Delta p)$ of the valve for any pressure drop Δp and spool angular position ϕ.

3.6.3. Reynolds number

To confirm the turbulent nature of an oil flow pattern in the valve for different spool angular positions, estimation of the Reynolds number Re has been performed according to the equations below:

$$\mathrm{Re} = \frac{\rho V L}{\mu} = \frac{VL}{\nu} \tag{15}$$

where V and L are characteristic velocity and length scales of the flow, ρ, μ and ν – fluid's density, dynamic and kinematic viscosity respectively, [34].

For circular conduits, the Reynolds number can be expressed through the volume flow rate Q, the flow area A and the hydraulic diameter D_h, which is the same as the pipe diameter or the characteristic length L, [35]. The more general formula for the hydraulic diameter, which accounts for noncircular pipes and hoses as the drop-shaped orifice, is

$$D_h = \frac{4A}{S} \tag{16}$$

where S is the perimeter of the flow cross-section. For the case of the initially chosen drop-shaped orifices, the total orifice perimeter S and area A were measured. The results are demonstrated in the figures 4 and 3 respectively. Therefore, it was possible to calculate the hydraulic diameter D_h of the orifice and use it further to estimate the Reynolds number.

The formula used for Reynolds number estimation is derived from the equation 15 through the hydraulic diameter D_h in equation 16 and the volume flow Q rate and the area A.

$$\mathrm{Re} = \frac{Q D_h}{A \nu} \tag{17}$$

The results of the Reynolds number calculations for different pressure differentials Δp and spool angular positions ϕ are illustrated in the Figure 9. The figure confirms, that for considered values of the valve opening and the pressure differential, the valve operates with the turbulent flow pattern since the Reynolds number exceeds the critical value of 2300 at almost all simulated design points.

It also can be concluded, that in the range of small valve openings, when the spool is positioned at $\phi < 30°$, the flow can take transitional nature in the throttling orifice areas as in this band the Reynolds number is within $1000<\mathrm{Re}<4800$.

3.6.4. Pressure losses

In order to estimate the pressure loss p_{loss} imposed by the valve to the hydraulic circuit it is installed in, another set of simulations has been conducted. In this case, the volume flow rate Q passing through the valve and the outlet pressure $p_{out} = 0.101\,325\,\mathrm{MPa}$ have been selected as the hydraulic boundary conditions. Volume flow rate here alters from $Q_{min} = 25\,\mathrm{l\,min^{-1}}$ to $Q_{max} = 275\,\mathrm{l\,min^{-1}}$ with a step of $Q_{step} = 25\,\mathrm{l\,min^{-1}}$. The spool angular position ranges from $\phi_{min} = 40°$ to $\phi_{max} = 90°$ with $\phi_{step} = 10°$. The measured goal is the magnitude of inlet pressure p_{in}. Hence, the pressure loss is defined by the difference

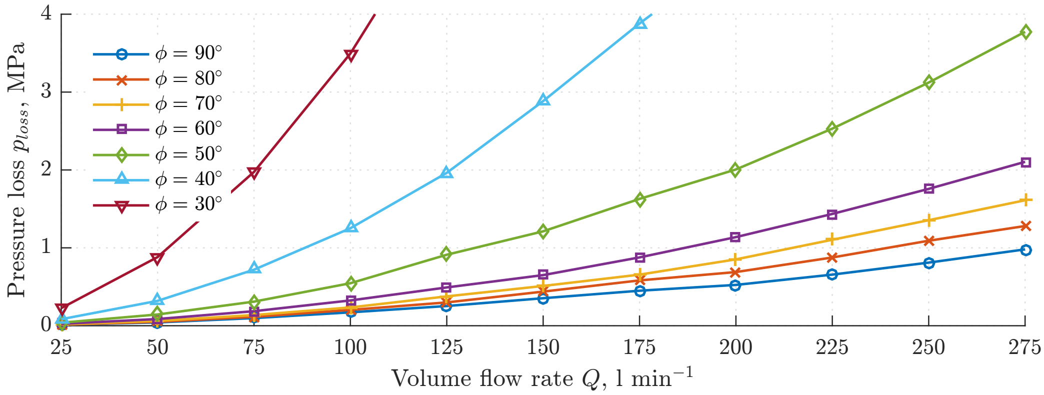

Figure 10: Modelled pressure losses $p_{loss}(Q)$ at ϕ = const.

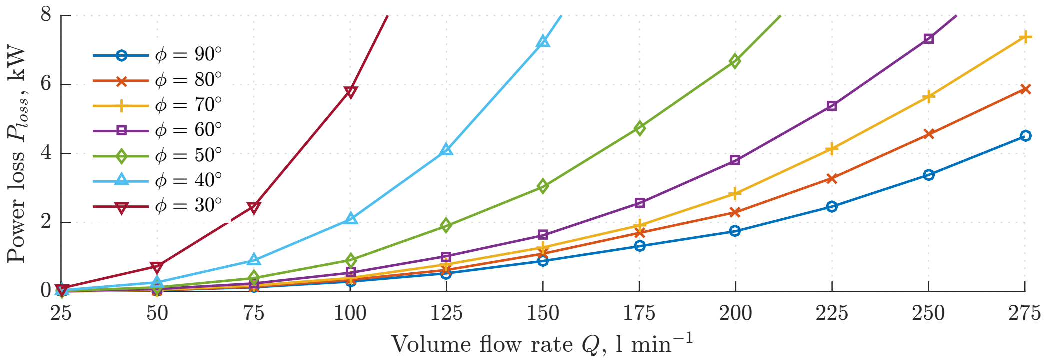

Figure 11: Modelled power losses $P_{loss}(Q)$ at ϕ = const.

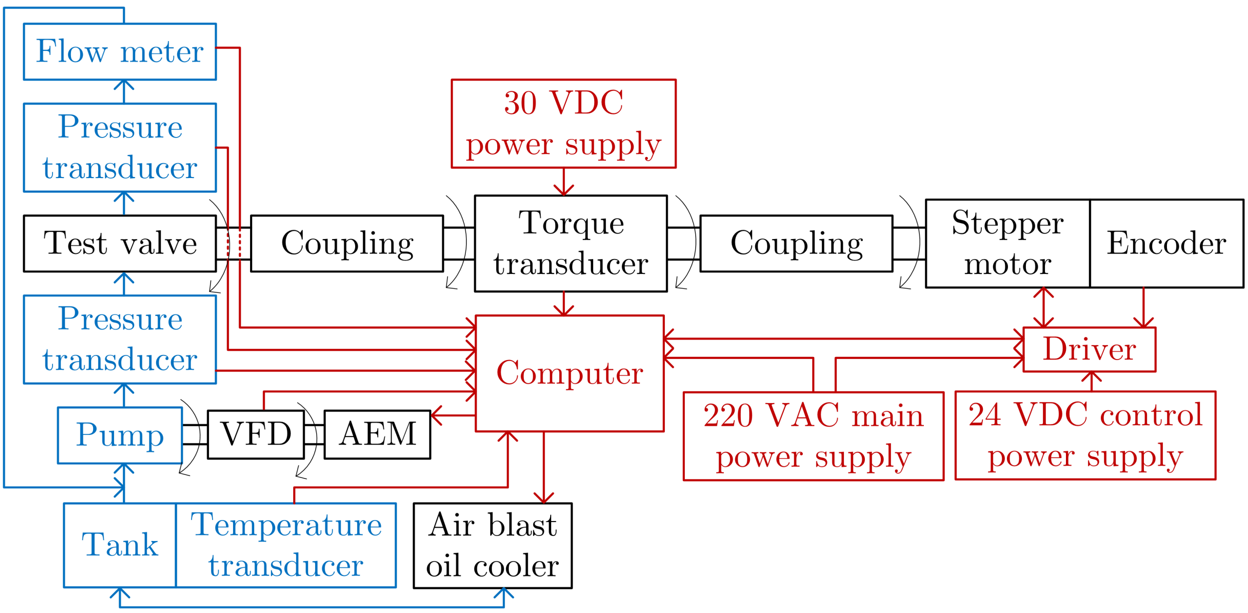

Figure 12: The block scheme of the data acquisition system. Blocks and signals colors correspond to: black – mechanical, blue – hydraulic, red – electric.

$$p_{loss} = p_{in} - p_{out}. \tag{18}$$

The resultant pressure loss curves, i.e. $p_{loss}(Q)$ at $\phi =$ const, for specified flow rates increase nonlinearly, with the dependency close to exponential. The maximum p_{loss} does not exceed 1 MPa at the fully open state of the valve and the maximum flow rate through it, i.e. at $Q(\phi_{max})$, see the figure 10.

$$P_{loss} = p_{loss}Q. \tag{19}$$

The obtained pressure loss function $p_{loss}(Q)$ allows further calculation of the power losses due throttling, see the figure 11, according to the formula below. This power is dissipated through oil viscous friction and increases the internal energy of the oil [1].

4. Experimental tests

A prototype of the valve was manufactured in order to test and validate the theoretical model of the valve described above. A detailed experimental procedure is designed to test the behaviour of the valve within the hydraulic system and test its modelling characteristics.

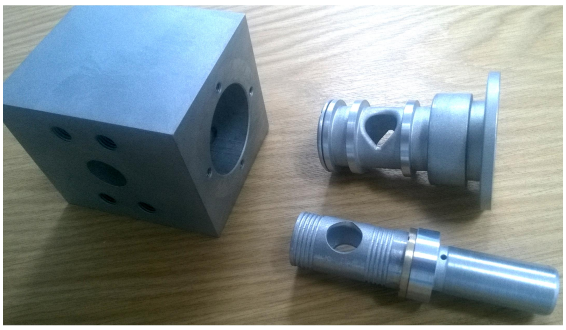

Figure 13: The main manufactured parts of the prototype valve: the valve body, the guiding sleeve inside the main sleeve, the spool with the thrust bearing on it.

4.1. Prototype valve

A physical prototype of the valve was manufactured by a contractor and assembled in accordance with the design specification described in the section 2. The prototype valve comprised original, standard and "off-the-shelf" parts.

Original parts include the RTSV's mechanical parts required to execute the new throttling method. These were manufactured in accordance with the design described above, see the figure 13.

However, a few geometrical simplifications of the valve parts were applied. Although the valve body's collecting channel in the prototype had a rectangular cross-section area A_{an}, the area was kept the same as in the original design specification, where the channel's shape corresponds to the one illustrated in the figure 1. Transition from the collecting channel to the outlet hydraulic port did not have a fillet on it. These deviations were considered as negligible and not influencing the overall valve performance. The overall length of the body was slightly shortened to reduce amount of the needed material. This resulted in small offset in the mounting threaded holes, which was taken into account during designing of the mounting base plate assembly described below.

4.2. Data acquisition system

The experimental data acquisition system (DAS) was used to collect data about the behaviour of the new valve in physical environment, as a part of a hydraulic system. The main purpose of the used DAS is to enable safe collection of the test data since the main component of the hydraulic is the mineral oil under high pressure.

DAS can be divided on three parts according to the physical nature of transmitted signals, see the figure 12. The mechanical component was described in the preceding sections. The details of the hydraulic test bench are discussed in the following section. Depending on the characteristic of interest, the monitored and controlled variables varied. Exact sets of monitored and controlled variable are summarized in the following experiment description.

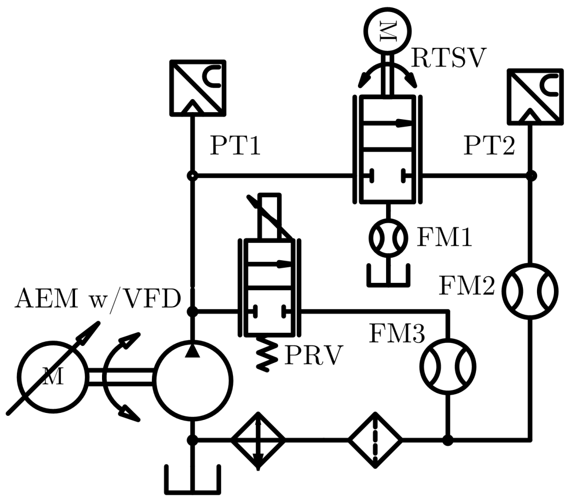

Figure 14: The scheme of the hydraulic test rig.

Instrument	Make	Model	Range	Accuracy
Pump	Hydreco	QR6 6160	Displacement $160\,\mathrm{cm^3\,rev^{-1}}$ Speed $450\,\mathrm{rev\,min^{-1}}$ to $2750\,\mathrm{rev\,min^{-1}}$	
FM	Kracht	VC12	$2\,\mathrm{l\,min^{-1}}$ to $600\,\mathrm{l\,min^{-1}}$ Resolution $83.33\,\mathrm{impulse\,rev^{-1}}$ Tooth volume $12\,\mathrm{cm^3}$	±0.3%
PT	Gems	3100B0400	400 bar Output 0.5 V to 4.5 V 4 mA to 20 mA	±0.25%
TT	HBM	T20WN	10 N m Output ±5 V 10 mA ± 8 mA	±0.5%
SM	Oriental Motors	RKS5913R	0.72° step	±0.05°

Table 2: Instrumentation.

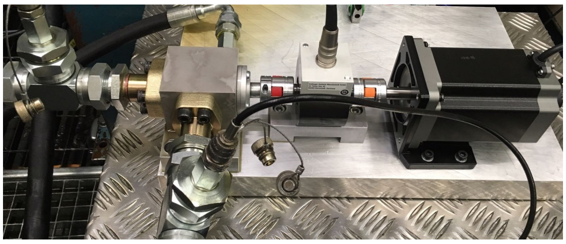

(a) The prototype valve, the RTSV.

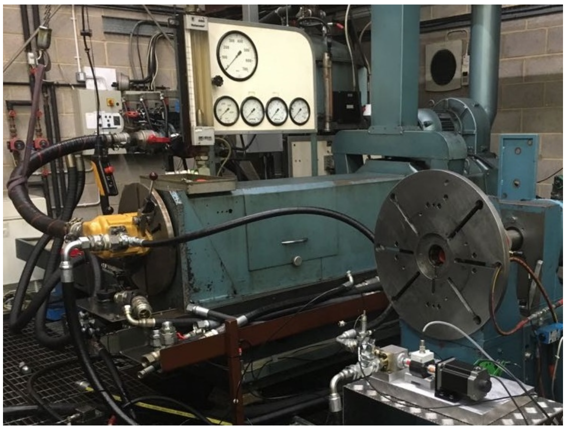

(b) The hydraulic test rig.

Figure 15: The photos of the used hydraulic test rig.

4.2.1. *Hydraulic test rig*

The figure 15 shows the image of the hydraulic test setup used for the experiments. It can be divided on the power, oil conditioning subsystems, sensors and the test prototype valve, RTSV. The figure 15a shows specifically the prototype valve, RTSV, and the figure 15b illustrates the general view on the used test rig.

The oil storing and conditioning subsystem included an oil tank with an inbuilt heater, oil filters, and an air blast heat exchanger. The tank also comprised a breather that connected the tank's chamber to surrounding environment to ensure that the atmospheric pressure level was maintained in the tank and the return line of the hydraulic system.

The power subsystem of the test rig was equipped with an asynchronous electric motor (AEM) with a variable frequency drive (VFD). The AEM served as a pump's driver, while the VFD allowed to set the rotational speed of the pump's shaft and, hence, to control the pump's volume flow rate supplied into the hydraulic system. The pump used here was a Hydreco's spur gear pump QR6 series with displacement of $160\,\mathrm{cm^3\,rev^{-1}}$, see the yellow-painted element in the figure 15b. Its operating speed range is $450\,\mathrm{rev\,min^{-1}}$ to $2750\,\mathrm{rev\,min^{-1}}$, [36].

In the power subsystem, in parallel to the pump, the was a pressure relief valve (PRV), which was installed in the by-pass line. The PRV is electronically controlled proportional valve, which allowed to set the valve's inlet pressure to the desired value. It also limited the pressure level in the hydraulic system, implementing the safety function. The by-pass line also included the flow meter FM3 to monitor the amount of flow passing through this line. The main hydraulic line incorporated the test valve, RTSV. The drain line of the RTSV featured the flow meter FM1 to measure the internal leak through the valve's parts. Up- and downstream to the prototype valve, two pressure transducers were mounted PT1 and PT2 respectively. Additionally, the flow meter FM2 was installed in the downstream of the test line to enable measuring the volume flow rate passing through the test valve.

4.2.2. *Instrumentation*

The oil's supply subsystem allowed keeping the temperature level constant in time. Thermocouples, the air-blast oil cooler and the heater formed the closed-loop temperature control system. The

Test	Variable	Type	Instrument	Range
$Q(\phi)$ at Δp = const	p_{in}	Controlled	VFD, PRV	0.35 MPa to 1.1 MPa
	ϕ	Controlled	SM	30° to 90°
	p_{out}	Monitored	PT2	40 MPa, see the table 2
	Q	Monitored	FM2	$600\,\mathrm{l\,min^{-1}}$, see the table 2
$\Delta p(Q)$ at ϕ = const	Q	Controlled	VFD, PRV	$25\,\mathrm{l\,min^{-1}}$ to $175\,\mathrm{l\,min^{-1}}$
	ϕ	Controlled	SM	50° to 90°
	p_{in}	Monitored	PT1	40 MPa, see the table 2
	p_{out}	Monitored	PT2	40 MPa, see the table 2

Table 3: Test plan.

tank-embedded thermocouples serving as temperature sensors allowed setting the temperature level on the same level throughout the length of an experiment. The working fluid was a zinc and chlorine free anti-wear hydraulic oil, Shell Tellus S2 V32 [37].

To monitor volume flow rates circulating the hydraulic system, three gear-type flow meters FM1, FM2 and FM3 were installed in the following hydraulic lines: pumps's by-pass, test valve's line and valve's internal leakage line. The latter enabled measurement of the oil spillage from the valve's central chamber, through the spool-sleeve gap and the thrust bearing to the tank. The leak drain line allows to lubricate all mechanical contacts within the valve with the working fluid, collect the leakage flow and direct it to the tank, see the figure 1.

The flow meters included two non-contacting measuring gears, which were driven by the liquid flow on a principle of a gear pump [38]. Apart from thermocouples and flow meters, the pressure sensors were used to collect the flow-related data, static pressure. The pressure transducers feature a sputter diaphragm, deformation of which is sensed and transformed into the pressure signal [39].

The used instrumentation is summarized in the table 2. According to the sensors' datasheets, accuracy of the used transducers can ensure a low systematic error of experiments.

4.3. Test procedures

The general goal during the design of the experiment stage was to replicate the valve metering characteristics obtained in the modelled environment. Test procedure development consisted of selecting and dividing the variables into controlling and recorded in order to enable recreation of the metering characteristics and, thereby, to meet the objective. The ranges of controlled variables corresponds to the boundary conditions used in the CFD parametric simulations for a particular metering function. The static parameters of interest are the volume flow rate, the pressure drop, leakages (internal and at the closed state). The summary of the test procedure is listed in the table 3. During all tests the temperature of oil was kept constant at 45 °C.

4.4. Tests results

The following sections report the results of the experiments conducted as a part of this investigation. The data collection was performed in according to the test plan, see the table 3. The figures shown below are the results of the static hydraulic representation of the proposed rotary flow control valve.

As a general note, visual inspection of the valve before, during and after each test did not reveal any leakages or visible deformations of the valve's parts. There were also no signs of rubber O-rings extrusions. The inspection allowed to conclude, that the valve was able to withstand highly pressurized oil without leakages and failure to operate. Therefore, the general design of the prototype was considered satisfactory and able to performs its functions.

4.4.1. Metering characteristic

During measurements of the volume flow rate characteristic of the valve $Q(\phi)$, the spool angular position was ranging from $\phi = 30°$ to $90°$. At every spool position ϕ, the PRV and the VFD were used to set the pressure differential across the valve equal to the values of $\Delta p = 0.25$ MPa, 0.5 MPa and 1 MPa. Then, the readings from the flow meter on the main line were recorded.

Experimental graphs of the volume flow rate as a function of the spool angular position are shown in the figure 16. These follow the same trend as the CFD modelled one, see the figure 7. However, the magnitudes differ drastically, especially for small valve openings and the low-opening spool positions, i.e. up

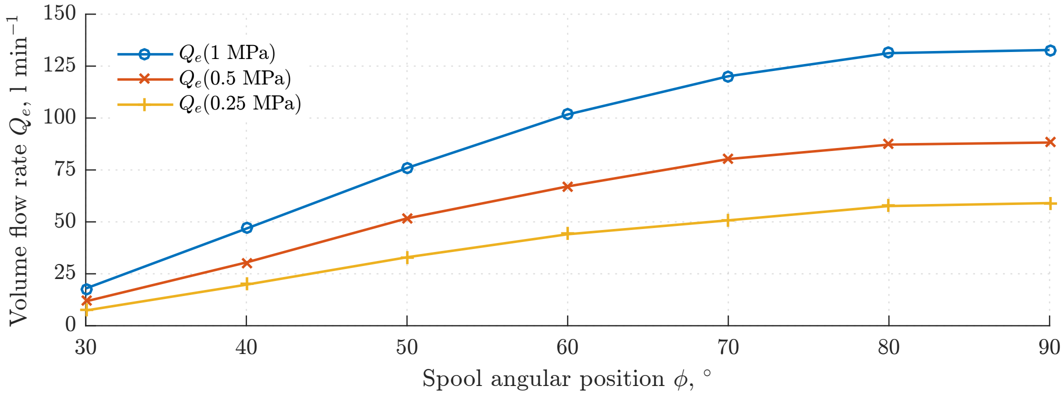

Figure 16: Tested metering characteristic $Q_e(\phi)$ at $\Delta p = 0.25;\ 0.5;\ 1$ MPa

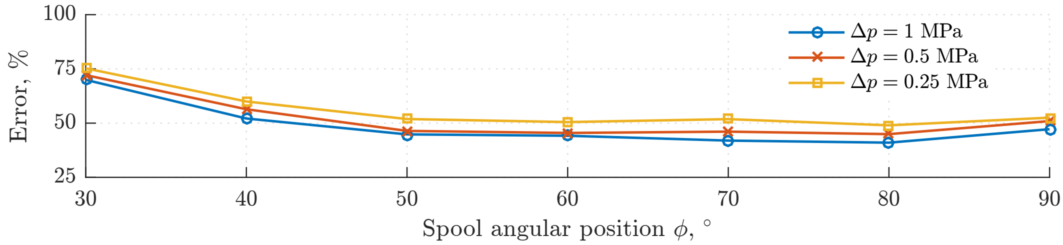

Figure 17: Percentage difference between simulated and tested metering characteristic $Q(\phi)$ at $\Delta p = 0.25;\ 0.5;\ 1$ MPa

to $\phi = 30°$, see the figure 17 showing the error between simulated and measured data.

According to the figure 17, the predicted values of the volume flow rate exceed the measured values by 48.75%, 51.77% and 55.85% in average for the three pressure drops of 1 MPa, 0.5 MPa and 0.25 MPa respectively. The error between the measured, see the figure 16, and modelled, see the figure 7, volume flow rates does not depend on the pressure drop causing the flow. That testifies to consistent data collection.

4.4.2. Pressure losses

During measurements of the pressure losses, VFD and PRV were simultaneously used to control the pump's discharge volume flow rate and the valve's inlet pressure respectively. The spool was put in the predetermined position in the range $\phi = 50°$ to $90°$ according to the test procedure. The spool openings below $\phi = 50°$ caused the inlet pressure to rise above 20 MPa, which was considered unsafe. The parameters monitored were the valve's outlet and inlet pressure levels. The difference between these values constituted the predicted pressure drop Δp, or the pressure loss.

The opposite tendency to the volume flow rate results was observed to the pressure drop curves. Here, the experimental values are higher than the modelled with a higher similar margin. The pressure measurements were performed with the maximum volume flow rate 175 l min^{-1}. Further increase in the volume flow rate led to the inlet pressure level rise above 20 MPa, which was considered risky in terms of structural integrity of the valve.

In case of pressure drop measurements, simulated and test results deviations differ, see the figure 19. The smaller valve openings result in the highest results error of 90.25% on average, i.e. in these cases experimental results are almost two times bigger than simulated, regardless of volume flow rate.

As the opening reaches maximum, the error decreases reaching 72.69% in the range of volume flow rates from 100 l min^{-1} to 150 l min^{-1}. At the fully open state and the minimal volume flow rate, the error is comparable with small opening's errors, i.e. 91.68%.

4.4.3. Correlation with modelling

According to the figures 17 and 19, the used simulation model overestimates the performance characteristics of the physical prototype valve on average by 82.78% in the case of the pressure drop test results. But general trends of the simulated

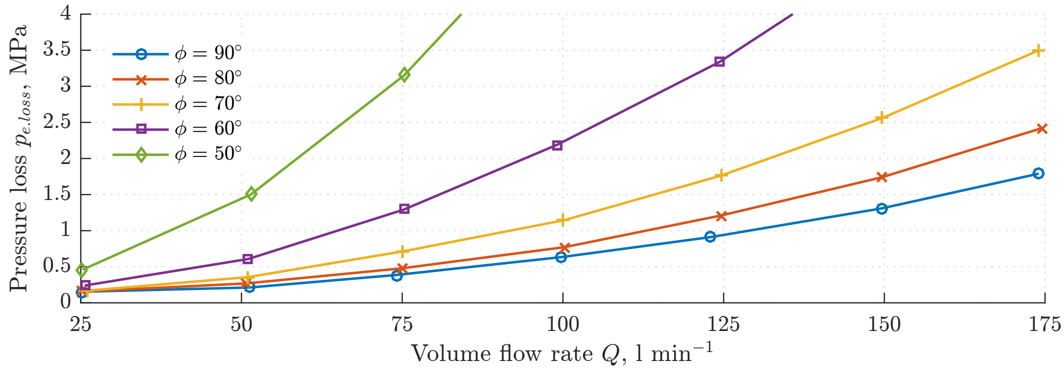

Figure 18: Tested pressure loss $p_{e.loss}$ at ϕ = const.

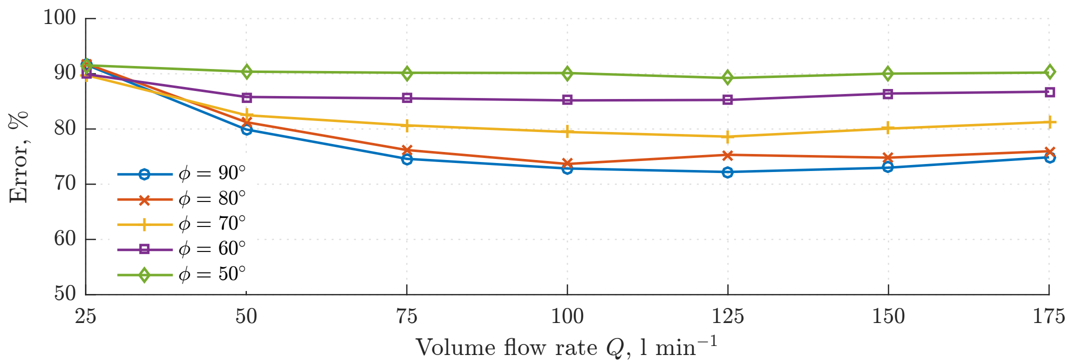

Figure 19: Percentage difference between modelled and tested pressure drops $\Delta p(Q)$ at ϕ = const.

and experimental results conform. In particular, the monotonous increase of the volume flow rate with valve opening for different values of constant pressure drops was observed. The pressure drops for a set value of the valve opening were raising with a volume flow rate growth. The linear proportionality of the leakage volume flow rate relatively to the pressure differential was confirmed.

Several factors were identified, which were causing such large errors. One factor affecting all measurements and all performed tests was related to the accuracy of the spool angular positioning. The prototype was assembled in a way that overlap angles at the closed state were impossible to measure and control. Hence, although the valve was closed, the exact lengths of the leak channels were hard to establish. Therefore, it was challenging to ensure that leak channels' lengths are equal to those used in the modelling stage. As a result, the actual "zero" position differed from the simulated. In addition, a signal noise caused by the high variability of the flow parameters in time and non-uniformity of the pump's flow rate also affects the quality of the collected data due to introduction of a random error.

However, the main reason of the tested and modelled results differences can be attributed to the imperfections of the geometric model used. Firstly, it did not include fittings into the model's geometry. These fittings connect the pressure transducers and the prototype valve to the hydraulic system. Their internal passages were non-uniform in a cross-section, their routes were not straight. Hence, their internal passages created additional disturbances to the flow, which were not accounted in the simulation model. This is the first factor causing a divergence of the modelled and experimental valve's metering characteristics.

Moreover, the simulated geometric model did not take into account surfaces roughness of mechanical parts wetted with oil. Surface's roughness creates additional pressure losses due to viscous and boundary layer-surface friction. Together, these two factors can explain the difference between experimental and simulated results. To test these assumptions, additional modelling was performed.

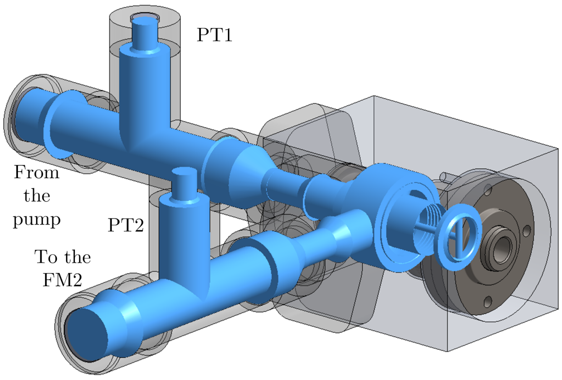

Figure 20: Corrected geometric model and fluid sub domain.

4.4.4. *Corrected model*

To test the assumptions made, an extra run of the hydraulic behaviour modelling was performed. In this simulation the geometric model was corrected to include the instrumentation's fittings, pressure transducers' ports and adapters, which served as transition from one internal nominal diameter to another, see the figure 20. These elements were created with the internal geometry as close as possible to those used in testing.

To fully replicate the geometry of the tested prototype, the solid model of the valve has been modified as well. In the manufactured prototype the annular collecting channel had a rectangular shape without fillets. Similarly the spool and sleeve orifices in the test valve had right edges, with no fillets. According to these deviations of the valve internal geometry from the design specification, modifications of the body, the sleeve and the spool were introduced. Adopted geometrical corrections resulted in the modified flow path, which reflected the test conditions more accurately.

Furthermore, roughness of $Ra25$ was assigned to all internal surfaces and passages, which are in contact with oil. The chosen roughness corresponds to finishing levels of the manufacturing processes used during prototype production – metal cutting with rough finish.

To study the influence of the corrected geometry on the pressure drop, the hydraulic problem with the following boundary conditions was solved: the spool angular position $\phi = 90°$, the volume flow rate range $Q = 25\,\mathrm{l\,min^{-1}}$ to $175\,\mathrm{l\,min^{-1}}$ and the the outlet static pressure $p_{out} = 0.101\,325\,\mathrm{MPa}$, the measured variable is the inlet pressure p_{in}. Then, the pressure difference Δp was calculated and plotted, see the figure 21.

According to the figure 21, correcting the geometric model of the prototype valve brought the simulation results much closer to the experiment results. Taken measures to modify simulations allowed to reduce the average error between modelling and experiment by 47.75%, from 77.02% to 29.27%, see the figure 22. Therefore, it can be concluded that the biggest factor contributing to the simulation and the experiment results deviations was caused by the incomplete geometric model and the "smooth wall" assumption.

After introduced modifications to the CFD settings (inclusion of the fittings to the valve geometric model and adding roughness to the internal surfaces), the percentage difference between the corrected simulation and the experimental results still remained quite large, average 29.27%, see the figure 22. Despite this error, the applied simulation model can be considered accurate enough to predict hydraulic behaviour of the tested prototype valve. The simulation results from the previous chapters can be deemed valid too and used in further performance improvement, design optimization, etc. The obtained metering characteristics from CFD modelling hold their relevance since they pertained to the valve geometry only, excluding the elements of the hydraulic test rig and used instrumentation.

5. Benchmark

As a benchmark valve, Tecnord's products were selected as the company is one of market leaders in hydraulic components design and production. Moreover, Tecnord's manual rotary spool valves SJ-MRA [40] represent the closest analogue to the developed valve both structurally and in terms of specification.

According to the data sheet, the valve is a two ways, two positions, proportional cartridge flow control valve with a rotary, tubular spool, see the figure 23. It has a cartridge-nest assembly method, the valve includes the movable hollow spool inside the static sleeve as the main throttling pair. The outside diameter of the sleeve in this valve is determined by the thread 1'' 5/16, which corresponds to 32 mm. The same outer sleeve diameter in the developed RTSV is 29.51 mm. The spool has two orifices, which are located opposite to each other. Its nominal volume flow rate is $151\,\mathrm{l\,min^{-1}}$, the rated operational pressure is 20.7 MPa. Despite many similarities, the Tecnord's valve is manually driven, which substantially limits its ability for fine control and, hence, its application area.

According to the performance data of this valve, in the fully open state at the rated flow rate of $150\,\mathrm{l\,min^{-1}}$ the created pressure drop by the valve makes up

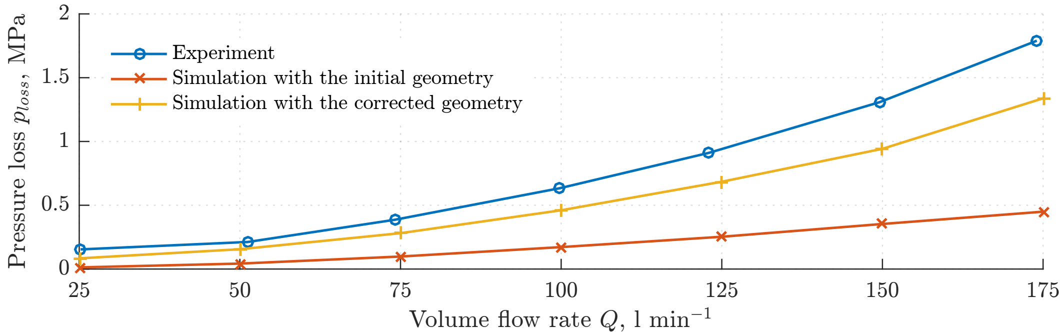

Figure 21: Correlation of study results for ϕ = 90°.

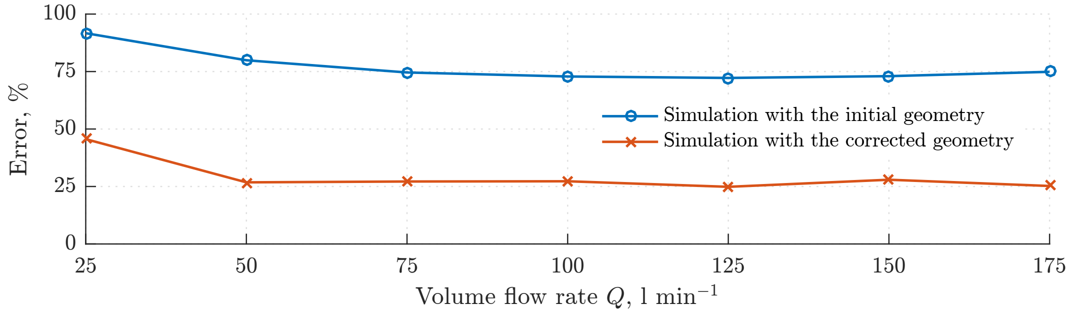

Figure 22: Percentage difference between simulated and test results of the pressure drop at ϕ = 90° relatively to the experiment data after inclusion of the test rig elements.

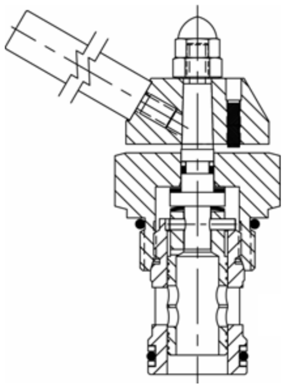

(a) Cross-section.

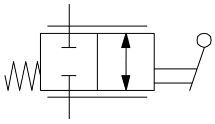

(b) Hydraulic symbol.

Figure 23: Tecnord's SJ-MRA rotary flow control valve, [40].

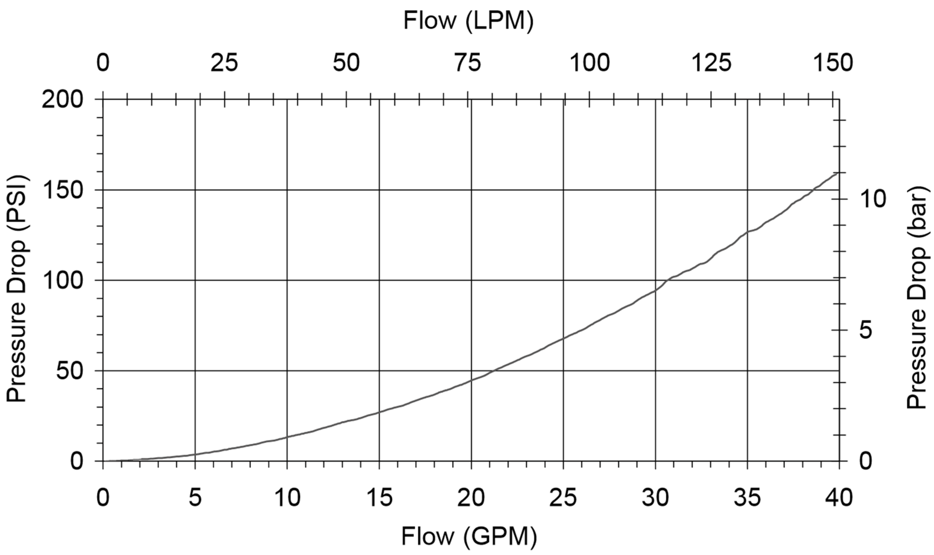

Figure 24: Test data of the pressure drop of SJ-MRA [40].

1.1 MPa. Whereas in the RTSV the corresponding pressure drop constitutes 0.35 MPa, see the figure 10, with 67.9% difference relatively to the Tecnord's valve. In this comparison, the simulated data for the valve

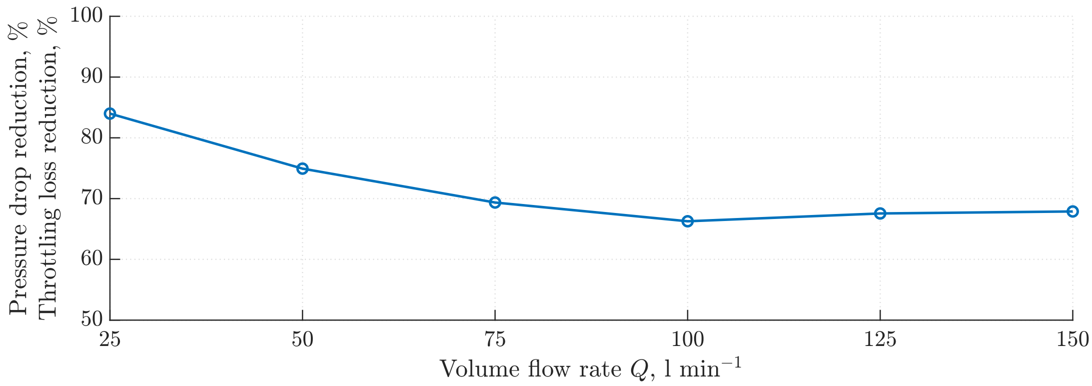

Figure 25: Throttling loss reduction in the RTSV relatively to the Tecnord's SJ-MRA.

geometry without the elements belonging to the test rig instrumentation was used. The comparison results are illustrated in the figure 25.

The calculated percentage of the average pressure drop reduction of 71.66% can be directly translated into the energy efficiency gain. Since the throttling power loss is proportional to the pressure drop, the curve in the figure 25 also corresponds to percentage of efficiency improvement relative to the Tecnord's reference valve.

6. Discussion

The performance evaluations during testing of the new valve, referred as the Rotary Tubular-Spool Valve (RTSV), allowed to validate the numerical models. The simulated performance characteristics of the valve agree well with experiments. The metering and pressure loss functions were derived from CFD modelling and tested. Therefore, the models could be further used to analyse other aspect of RTSV's functionalities.

The simulation results confirmed the that developed RTSV can successfully perform the required functions of a flow control valve in hydraulic systems and, thereby control the speed of a hydraulic actuator and a rotary motor.

Although the benchmark performance comparison study showed significant increase in energy efficiency of the new valve, it can differ for other valves designed by other manufacturers. Nevertheless, the obtained results confirm the potential of the new valve to become the industry standard, to replace single-spool valves with the independent metering arrangement of RTSVs to control the actuator's speed.

7. Conclusion

The objective of this research was met by investigating the three-dimensional fluid dynamics of internal flows within the valve to determine the initial metering characteristics and pressure losses it creates. The simulation results demonstrated RTSV's flow control feasibility as well as its ability to operate in the high-flow rate operational domain, with the volume flow rate reaching 250 l min^{-1} at 1 MPa pressure differential. At the fully open state and the rated volume flow rate, valve's pressure drop was 0.81 MPa. Its performance was deemed comparable with industry available valves and having great potential to compete with benchmark hydraulic components.

The experimental investigation focused on characterising the RTSV's hydraulic performance. The prototype valve was built according to the suggested design concept. The test rig and the data acquisition system were designed, its elements were acquired and assembled. These enabled to replicate simulation set-up and collect data pertaining to performance characteristics, which had been simulated simulated before.

Manufacturing and testing of the prototype proved its relative design simplicity and modelled strength, its ease of manufacture and operation. The results of tests, although differing from initial simulations in average by 52.12% for the volume flow rate function and by 82.78% for pressure drops, followed same trends as modelled. The factors causing the error were identified. To address these factors, the CFD modelling settings were corrected. These corrections to the model significantly reduced simulation/experiment errors in average by 47.75% for the pressure drop function. Thereby the initial simulation results were validated.

The comparison study with the selected industrially available flow control valve having the similar structure and performance proved superior qualities of the developed RTSV. The ability of the novel valve to improve energy efficiency of hydraulic control system was demonstrated by evaluating and comparing throttling losses occurring in the RTSV and the reference valve. The average pressure drop reduction of the RTSV amounted to 71.66%.

References

[1] Merritt, Herbert E., Hydraulic Control Systems, John Wiley & Sons, Inc., New York, 1968.

[2] B. Eriksson, Mobile Fluid Power Systems Design with a Focus on Energy Efficiency, Doctoral dissertation, Linkopings University (2010).

[3] C. Burrows, Fluid power–some reflections, in: The 6th International Conference on Hydraulic Machinery and Hydrodynamics, no. February, Timisoara, Romania, 2004, pp. 51–56.

[4] M. Axin, Mobile Working Hydraulic System Dynamics, Dissertation, Linköping University (2015).

[5] P. Tamburrano, A. Plummer, E. Distaso, R. Amirante, A review of direct drive proportional electrohydraulic spool valves: Industrial state-of-the-art and research advancements, Journal of Dynamic Systems, Measurement and Control, Transactions of the ASME 141 (2). doi:10.1115/1.4041063.

[6] E. Lisowski, W. Czyzycki, J. Rajda, Three dimensional CFD analysis and experimental test of flow force acting on the spool of solenoid operated directional control valve, Energy Conversion and Management 70 (2013) 220–229. doi:10.1016/j.enconman.2013.02.016.

[7] P. Bordovsky, K. Scmitz, H. Murrenhoff, CFD Simulation and Measurement of Flow Forces Acting on a Spool Valve, in: 10th International Fluid Power Conference, Dresden, Germany, 2016, pp. 473–484.

[8] N. Herakovič, CFD simulation of flow force reduction in hydraulic valves, Tehnicki vjesnik - Technical Gazette 22 (2) (2015) 453–463. doi:10.17559/TV-20141128090939.

[9] E. Lisowski, G. Filo, Analysis of a proportional control valve flow coefficient with the usage of a CFD method, Flow Measurement and Instrumentation (February) (2016) 1–10. doi:10.1016/j.flowmeasinst.2016.12.009.

[10] E. Lisowski, G. Filo, CFD analysis of the characteristics of a proportional flow control valve with an innovative opening shape, Energy Conversion and Management 123 (2016) 15–28. doi:10.1016/j.enconman.2016.06.025.

[11] E. Lisowski, G. Filo, J. Rajda, Analysis of flow forces in the initial phase of throttle gap opening in a proportional control valve, Flow Measurement and Instrumentation 59 (2018) 157 – 167. doi:https://doi.org/10.1016/j.flowmeasinst.2017.12.011. URL http://www.sciencedirect.com/science/article/pii/S095559861730331X

[12] M. Rabie, Fluid Power Engineering, McGraw-Hill Education, 2009.

[13] J. Yu, J. Zhuang, D. Yu, Modeling and analysis of a rotary direct drive servovalve, Chinese Journal of Mechanical Engineering 27 (5) (2014) 1064–1074. doi:10.3901/CJME.2014.0725.127. URL https://doi.org/10.3901/CJME.2014.0725.127

[14] H. Wang, G. Gong, H. Zhou, W. Wang, Steady flow torques in a servo motor operated rotary directional control valve, Energy Conversion and Management 112 (2016) 1–10. doi:10.1016/j.enconman.2015.11.054.

[15] M. Zhu, S. Zhao, J. Li, Design and analysis of a new high frequency double-servo direct drive rotary valve, Frontiers of Mechanical Engineering 11 (4) (2016) 344–350. doi:10.1007/s11465-016-0406-x. URL https://doi.org/10.1007/s11465-016-0406-x

[16] M. Zhu, S. Zhao, J. Li, P. Dong, Computational fluid dynamics and experimental analysis on flow rate and torques of a servo direct drive rotary control valve, Proceedings of the Institution of Mechanical Engineers, Part C: Journal of Mechanical Engineering Sciencedoi:10.1177/0954406218756449.

[17] M. Zhu, S. Zhao, P. Dong, J. Li, Design and analysis of a novel double-servo direct drive rotary valve with high frequency, Journal of Mechanical Science and Technology 32 (9) (2018) 4313–4323. doi:10.1007/s12206-018-0829-x. URL https://doi.org/10.1007/s12206-018-0829-x

[18] E. Husley, Rotary control valve, US3135293A (1962).

[19] R. Erwin, E. Husley, Rotary sleeve valves, US3005468A (1958).

[20] Ivan Okhotnikov, Siamak Norooz, Philip Sewell, Philip Godfrey, Evaluation of steady flow torques and pressure losses in a rotary flow control valve by means of computational fluid dynamics, International Journal of Heat and Fluid Flow 64 (2017) 89–102. doi:https://doi.org/10.1016/j.ijheatfluidflow.2017.02.005.

[21] D. C. Wilcox, Turbulence Modeling for CFD, 3rd Edition, DCW Industries, Inc, 2006.

[22] SolidWorks, SolidWorks Flow Simulation (2015).

[23] A. Palumbo, R. Paoluzzi, M. Borghi, M. Milani, Forces on a hydraulic valve spool, Proceedings of the JFPS International Symposium on Fluid Power 1996 (3) (1996) 543–548. doi:10.5739/isfp.1996.543.

[24] SolidWorks, Enhanced Turbulence Modeling in SolidWorks Flow Simulation (2013).

[25] C. K. G. Lam, K. Bremhorst, A Modified Form of the $k-\varepsilon$ Model for Predicting Wall Turbulence, Journal of Fluids Engineering 103 (3). doi:10.1115/1.3240815.

[26] A. Sobachkin, G. Dumnov, Numerical Basis of CAD-Embedded CFD, NAFEMS World Congress 2013 February (2013) 1–20.

[27] Launder, B.E. E. and Spalding, D.B. B., The numerical computation of turbulent flows, Computer Methods in Applied Mechanics and Engineering 3 (2) (1974) 269–289.

[28] E. R. V. Driest, On Turbulent Flow Near a Wall, Journal of the Aeronautical Sciences 23 (11) (1956) 1007–1011. doi:10.2514/8.3713.

[29] SolidWorks, Advanced Boundary Cartesian Meshing Technology in SolidWorks Flow Simulation (2013).

[30] T. Dell, Load-Sensing Pressure-Compensating (LSPC) Hydraulic Systems, in: Hydraulic Systems for Mobile Equipment, Goodheart-Willcox, 2017, Ch. 18.

[31] B. Nielsen, Controller Development for a Separate Meter-In Separate Meter-Out Fluid Power Valve for Mobile Applications, Ph.D. thesis, Aalborg University (2005).

[32] H. Ji, Y. Cao, Z. Wang, Y. Wang, Numerical analysis of temperature rise by throttling and deformation in spool valve, Proceedings of 2011 International Conference on Fluid Power and Mechatronics, FPM 2011 (2011) 752–756doi:10.1109/FPM.2011.6045861.

[33] CITGO, Product Information. CITGO A/W Hydraulic oils (2015).

[34] F. White, Fluid Mechanics, the fourth Edition, McGraw-Hill series in mechanical engineering, 1999.

[35] W. Durfee, Z. Sun, Fluid Power System Dynamics, Center for

Compact and Efficient Fluid Power (CCEFP), Department of Mechanical Engineering, University of Minnesota, 2009.

[36] Hydreco, Q Series Hydraulic Gear Pumps (2017). URL https://www.hydreco.com/info-downloads/technical-data-sheets/

[37] Shell, Industrial Hydraulics Fluid Shell Tellus S2 V32 (2017). URL http://www.epc.shell.com/

[38] Kracht, Gear Type Flow Meter VC (2017). URL http://www.krachtcorp.com/wp-content/uploads/2012/05/VC_USA_02-12_view.pdf

[39] Gems, 3100 Series and 3200 Heavy Duty Series Compact OEM Pressure Transmitters (2017). URL https://www.gemssensors.co.uk/~/media/files/resources/na_english/catalogpages/catalog-h_3100series-3200series.ashx

[40] Tecnord, SJ-MRA Manual Rotary Spool Valve, 2 Way (2017). URL https://www.tecnord.com/tabelle/cartridge-valves/mechanical-directional-pdf/SJ-MRA.pdf